



Extreme Precipitation in the West African Cities of Dakar and Ouagadougou: Atmospheric Dynamics and Implications for Flood Risk Assessments

THOMAS ENGEL,^a ANDREAS H. FINK, PETER KNIPPERTZ, AND GREGOR PANTE

Institute of Meteorology and Climate Research, Karlsruhe Institute of Technology, Karlsruhe, Germany

JAN BLIEFERNICHT

Institute of Geography, University of Augsburg, Augsburg, Germany

(Manuscript received 3 September 2016, in final form 28 June 2017)

ABSTRACT

Two extreme, high-impact events of heavy rainfall and severe floods in West African urban areas (Ouagadougou on 1 September 2009 and Dakar on 26 August 2012) are investigated with respect to their atmospheric causes and statistical return periods. In terms of the synoptic–convective dynamics, the Ouagadougou case is truly extraordinary. A succession of two slow-moving African easterly waves (AEWs) caused record-breaking values of tropospheric moisture. The second AEW, one of the strongest in recent decades, provided the synoptic forcing for the nighttime genesis of mesoscale convective systems (MCSs). Ouagadougou was hit by two MCSs within 6 h, as the strong convergence and rotation in the AEW-related vortex allowed a swift moisture refueling. An AEW was also instrumental in the overnight development of MCSs in the Dakar case, but neither the AEW vortex nor the tropospheric moisture content was as exceptional as in the Ouagadougou case. Tropical Rainfall Measuring Mission (TRMM) 3B42 precipitation data show some promise in estimating centennial return values (RVs) using the “peak over threshold” approach with a generalized Pareto distribution fit, although indications for errors in estimating extreme rainfall over the arid Sahel are found. In contrast, the Precipitation Estimation from Remotely Sensed Information Using Artificial Neural Networks–Climate Data Record (PERSIANN-CDR) dataset seems less suitable for this purpose despite the longer record. Notably, the Ouagadougou event demonstrates that highly unusual dynamical developments can create extremes well outside of RV estimates from century-long rainfall observations. Future research will investigate whether such developments may become more frequent in a warmer climate.

1. Introduction

Extreme rainfall events frequently cause flash floods in Africa with devastating consequences for residents, agriculture, and infrastructures, as they often occur with little warning. Between 1981 and 2014, more than 3000

people died, nearly half a million lost their homes, and more than 2.3 million people were affected by flash floods (EM-DAT 2015; see also Jonkman 2005). In 2007, 45 flood events in Africa killed 869 people and nearly 2.5 million were displaced (DFO 2015). During a flooding episode in September 2009, more than 600 000 people in 16 West African nations were affected (World Water Assessment Programme 2009), with at least 32 killed in Burkina Faso and Ghana (BBC News 2009).

Urban areas are particularly vulnerable to sudden inundations. Buildings, roads, and pavements lead to a compaction and sealing of soils, such that rainwater is unable to infiltrate and therefore accumulates at the surface. During intense thunderstorms, this can create rapid currents within a short time. In addition, insufficient urban planning urges poor people to settle in flood-prone areas of cities (Hardoy et al. 2001; Nchito 2007;

Denotes content that is immediately available upon publication as open access.

Supplemental information related to this paper is available at the Journals Online website: <https://doi.org/10.1175/JHM-D-16-0218.s1>.

^a Current affiliation: Comsoft Solutions GmbH, Karlsruhe, Germany.

Corresponding author: Andreas H. Fink, andreas.fink@kit.edu

Douglas et al. 2008) with insufficient infrastructure, canalization, and waste removal. In addition, standing water favors outbreaks of waterborne diseases such as cholera (IPCC 2007), and flood damages entail shortages in the food supply (Hartill 2008).

Both demographic and climatic factors could exacerbate this situation in the future. Enormous population growth and urbanization occurred in Africa in recent decades and are projected to continue. Since 1950 the population quadrupled and is likely to quadruple again until the end of the twenty-first century, with then more than 4 billion inhabitants (UNDP 2015). In 2050 more than 1.3 billion are expected to live in urban areas—5 times more than in 2000 (UNDP 2015). In addition, Africa has been identified as the region most vulnerable to climate change and variability (IPCC 2012). For African countries, impacts of natural hazards are projected to be 20–30 times larger than in industrialized countries (IPCC 2014). The most severe climate change impacts can be expected for regions of high population density and poverty rates (Müller et al. 2014), as often observed in African cities. Hirabayashi et al. (2013) found a high consistency among global climate models predicting large increases in flood frequency in Africa under the strongest climate change scenario RCP8.5.

Despite this worrying situation, there is a relatively limited body of scientific work on extreme rainfall events that lead to flooding in West Africa, particularly in urban areas. Tarhule (2005) surveyed 79 damaging rainfall events between 1970 and 2000 in Niger based on newspaper accounts and states that not only the intensity of a single heavy rainfall event but also the cumulative rainfall of the preceding days determines the probability of inundations. Paeth et al. (2011) examined the causes of the 2007 flood in the northern parts of sub-Saharan Africa that affected more than 1.5 million people. Large parts of West Africa had the most intense rainfall in several decades in this year, and in the upper Volta basin 3-day accumulated precipitation amounts with return periods of more than 1000 years occurred.

To improve early warning systems and to develop mitigation strategies, detailed studies of extreme rainfall that led to flooding events are needed. However, adequate observational rainfall data are often lacking in Africa (e.g., Nicholson et al. 2003). The coverage of rain gauges is low (~ 1 for every 5000 km^2) and even shrinking in recent decades; data quality is sometimes questionable because of outdated instrumentation and manual readings. Frequent coding errors lead to erroneous extreme daily rainfall amounts, which do not get eliminated by simple quality controls in widely used datasets such as the NOAA Integrated Surface Database (<https://www.ncdc.noaa.gov/isd>). Without nearby

stations, it is often impossible to distinguish erroneous data from real events with centennial return periods. Since the advent of geostationary satellites around the 1980s and subsequently the launch of the Tropical Rainfall Measuring Mission (TRMM) satellite in 1997, daily satellite-based rainfall estimations (SRFEs) have opened new avenues for quality checks of gauge data. However, these SRFEs are based on proxies related to radiative and emissive properties of cloud hydrometeors at visible, infrared, and microwave wavelengths. In addition, the infrared-based SRFE time series starting in the 1980s were affected by inhomogeneities due to many changes in satellite instrumentation.

The present study investigates two recent, high-impact urban flooding events in West Africa: the Ouagadougou flood in September 2009 and the Dakar flood in August 2012. It takes advantage of a combination of factors to detail the synoptic–dynamic evolution and to infer robust statistical return values for these events: 1) most importantly, ~ 100 -yr-long time series of daily rainfall with very few gaps are available at both locations—a very rare situation in Africa, and 2) recently, the Precipitation Estimation from Remotely Sensed Information Using Artificial Neural Networks–Climate Data Record (PERSIANN-CDR; Ashouri et al. 2015), a homogenized, 32-yr-long (1983–2014) SRFE dataset, was released. The PERSIANN-CDR algorithm uses homogenized infrared brightness temperatures and was trained in a neural network approach with a high-quality, high-resolution, blended radar–gauge dataset over the United States.

PERSIANN-CDR daily rainfall estimates and derived return periods for the two extreme rainfall events under study will be compared to estimates from gauge and the 17-yr (1998–2014) TRMM 3B42 data (Huffman et al. 2007) to test the usefulness of the two SFRE datasets for estimating flood risks in urban areas with shorter or no daily gauge data. In addition, the present pilot study will discuss the characteristics and hitherto poorly documented atmospheric dynamics of these events. Only the Ouagadougou rainfall event is briefly discussed in Cornforth et al. (2017) as an example of an African easterly wave (AEW) breaking event, and a synoptic overview is given in Galvin (2010).

The paper is structured as follows. Section 2 gives a detailed description of the gauge, satellite, and re-analysis data used in this study, including their advantages and limitations. Section 3 describes the methods to diagnose convective dynamics as well as some statistical tools. The analysis of the atmospheric dynamics of the two selected cases will be presented in section 4, while section 5 will provide the results of the statistical evaluation of the long-term context. Section 6 summarizes

our findings with concluding remarks and an outlook on future investigations.

2. Data

a. Gauge data

Rain gauges are the most reliable method of measuring the precipitation amount and offer a high temporal resolution. In general, the availability of high-quality, long-term daily rainfall records is rather limited in Africa. However, the two extreme events considered affected two major West African urban areas, for which long time series of daily rainfall could be constructed by filling in data gaps and extending the series back in time using stations within a radius of 10 km around the synoptic stations Ouagadougou Aéro (12.35°N, 1.52°W, WMO ID 65503, 1902–2014, 113 years) and Dakar-Yoff (14.73°N, 17.5°W, WMO ID 61641, 95 years, 1919–2014) (for locations see Fig. 1a). While for Dakar only one rain gauge was available to the authors for the extreme event in August 2012, 42 additional stations with more than 80% of daily rainfall observations during the period 1983–2010, and thus including the September 2009 event, were available for Burkina Faso. These Burkinabe data were collected in the framework of the West African Science Service Center on Climate Change and Adapted Land Use (WASCAL) project (www.wascal.org) and consist of synoptic, agrometeorological, and stand-alone rain gauge stations. After quality checks, nine stations, including Ouagadougou Aéro, located in the quadratic regions 1–3 were available to conduct additional gauge–SRFE comparisons for areas of different sizes and station densities (Fig. 1b and online supplement to this article). Note that the synoptic stations report the 24-h rainfall between 0600 and 0600 UTC, while the additional Burkinabe stations usually report between 0800 and 0800 UTC.

b. Reanalysis data

The synoptic–dynamic analysis of the two heavy precipitation events is based on 6-hourly data of temperature, wind, and humidity from the European Centre for Medium-Range Weather Forecasts (ECMWF) interim reanalysis (ERA-Interim, hereafter ERA-I; Dee et al. 2011). ERA-I covers the time period from 1979 to present with a horizontal resolution of $0.75^\circ \times 0.75^\circ$ latitude–longitude and 60 vertical levels up to 0.1 hPa. The events will be assessed with regard to their anomalous total precipitable water (TPW) content with respect to the 1979–2014 period. Cook and Vizy (2015) found suspicious upward trends in the TPW over the Sahara and global tropics in the NCEP-2 and MERRA

reanalyses, but not in ERA-I. The latter has been verified for the Dakar and Ouagadougou area (not shown).

c. Satellite data

In large parts of Africa, where the coverage of weather stations is low, SRFEs offer the only possibility to obtain area-wide observations of precipitation. We have opted to test the allegedly best rainfall product at daily time scales, the TRMM 3B42 product, together with the recently released long-term PERSIANN-CDR.

1) TRMM

TRMM was launched on 27 November 1997 with the Visible and Infrared Scanner (VIRS; 5 channels), TRMM Microwave Imager (TMI; 9 channels), and Precipitation Radar (PR) instruments on board (Huffman et al. 2007). It has revolutionized the observation of precipitation from satellites and has become a standard data source for weather forecast and climatological purposes. The product 3B42 is based on 3-hourly estimates of precipitation rates with $0.25^\circ \times 0.25^\circ$ latitude–longitude resolution obtained from the combination of the three TRMM sensors mentioned above as well as microwave and infrared sensors aboard other satellites. The satellite-derived 3-hourly precipitation estimates are bias corrected with monthly surface observations from gauge stations. After more than 17 years, TRMM went out of operation in April 2015. In this study, the latest version 3B42 V7 is used for the period 1998–2014.

Several studies have confirmed a good performance of the TRMM algorithm in West Africa. Roca et al. (2010) and Gosset et al. (2013) demonstrated that the TRMM 3B42 V6 product belonged to the best-performing SRFEs at daily time scales when compared to rain gauge data from two well-instrumented sites in West Africa, the Sahelian Niamey (Niger) and the Soudanian Upper Ouéme Valley (Benin) site. This statement also holds for subdaily time scales, as was recently shown in Pfeifroth et al. (2016) for the same well-gauged mesosites. In a recent review paper, Maggioni et al. (2016) refer to additional studies that highlight the superiority of TRMM 3B42 V6 over other SRFEs in East and West Africa at daily time and 0.25° spatial scales. It is reasonable to assume that this finding also holds for version 7 (V7) used in the present study, as Zulkafli et al. (2014) and Prakash et al. (2015), for example, provide evidence that V6 and V7 are rather comparable.

2) PERSIANN-CDR

Ashouri et al. (2015) recently published the PERSIANN-CDR dataset of daily precipitation estimates with $0.25^\circ \times 0.25^\circ$ latitude–longitude spatial resolution

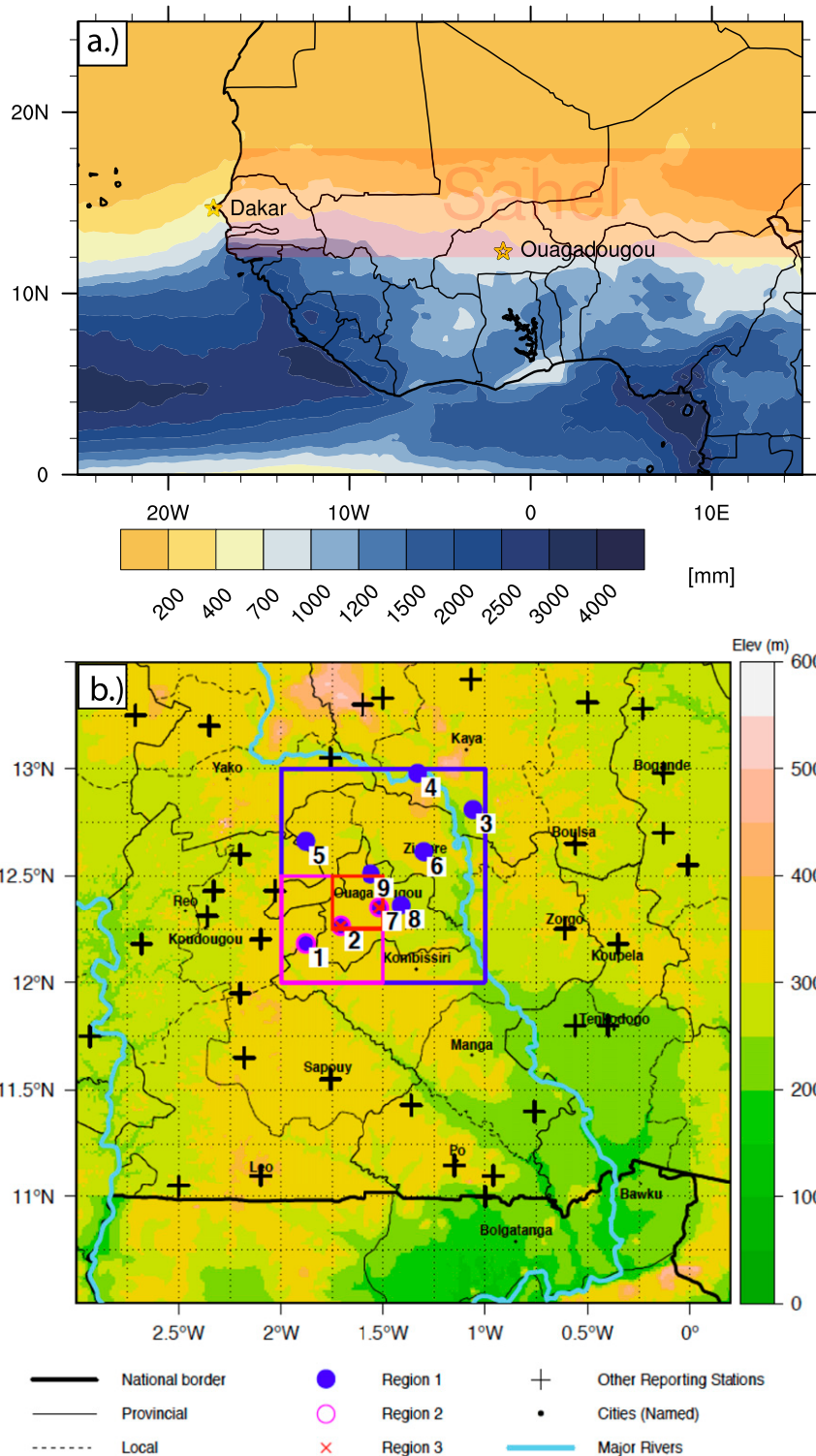


FIG. 1. Geographical overview and rainfall stations used in the study. (a) Annual precipitation (mm) averaged over 1998–2014 from TRMM 3B42. The light red shaded area shows the Sahel zone. The yellow stars indicate locations of Dakar and Ouagadougou. (b) Regions and additional rain gauge network used in Burkina Faso for 1980–2010. The stations with numbers 1–9 are listed in Table S1. Station 7 is Ouagadougou Airport.

from 1983 onward. An artificial neural network (ANN; Hsu et al. 1997, 1999) that is trained with radar and rain gauge data is applied to homogenized infrared (10.2–11.2 μm) brightness temperatures of GridSat-B1 (Knapp et al. 2011) and adjusted on a monthly basis to precipitation estimates for each $2.5^\circ \times 2.5^\circ$ latitude–longitude grid box of the Global Precipitation Climatology Project (GPCP; Huffman et al. 1997, 2001, 2009; Adler et al. 2003). The extended time period and relatively high spatial resolution makes PERSIANN-CDR advantageous for climatological studies compared to other satellite products. Ashouri et al. (2015) found a good performance of PERSIANN-CDR for Hurricane Katrina in 2005 and the Sydney flood in 1986 as compared to gauge and radar observations. Miao et al. (2015) showed a good performance in capturing spatiotemporal patterns of heavy rainfall in the eastern China monsoon region with a slight underestimation of the annual maximum of 1-day precipitation amounts. Two aspects are worthy of note: first, the daily accumulation period of PERSIANN-CDR is 0000–0000 UTC; thus, it is shifted by 6 h when compared to the 0600–0600 UTC accumulation period used for the surface gauge and TRMM 3B42 data. Second, many previous studies using PERSIANN data over Africa employed an earlier version, in which infrared brightness temperatures were trained with TRMM radar data (e.g., Gosset et al. 2013; Pfeifroth et al. 2016). The period used in the present study is 1983–2014.

3. Methods

a. Analysis of atmospheric dynamics

Both Ouagadougou and Dakar are located in the Sahel, a region stretching between about 12° and 18°N from the Atlantic coast to the Red Sea (see Fig. 1a). This area is characterized by the transition from the arid conditions of the Sahara with less than 200 mm rainfall per year to a more humid climate equatorward. The West African monsoon (WAM; e.g., Lafore et al. 2011) provides precipitation during the rainy season between June and September. Recent rainy seasons were characterized by frequent flooding like the 2007, 2010, and 2012 events (Paeth et al. 2011; Njau and Thiaw 2011; Sima et al. 2013). This is reflected in the findings of Sanogo et al. (2015), who found that the recent upturn in WAM rainfall is associated with a statistically significant increase in extreme precipitation events.

Large MCSs account for up to 90% of total rainfall in the Sahel (Lebel et al. 2003). Elongated linear or bow-shaped bands of heavy precipitation are often embedded in such systems. These “squall lines” usually

travel west-southwestward, perpendicular to their principal axis, at a speed of $\sim 50 \text{ km h}^{-1}$ and consist of a long leading band of intense convective precipitation about 50 km wide and several hundred kilometers long, with peak rain rates exceeding 100 mm h^{-1} , followed by a more extensive stratiform part with moderate rain (Rowell and Milford 1993; Lafore et al. 2017). Because of the small width of the convective part and the fast propagation of squall lines, high intensities are observed for only 10–20 min at a given location (Lafore et al. 2017), such that total rainfall is mostly in the range of 20–50 mm and rarely exceeds 100 mm (cf. Fink et al. 2017).

Such systems require large amounts of atmospheric humidity, which originate either from advection of moist air from the Atlantic Ocean or, to a lesser extent, from evaporation at the continental surface. A convergent humidity flux $q \cdot \mathbf{V}_h$ [with the specific humidity q (kg kg^{-1}) and horizontal wind vector \mathbf{V}_h (m s^{-1})] then causes an accumulation of moisture in the atmospheric column as TPW (kg m^{-2}):

$$\text{TPW} = \frac{1}{g} \int_{p_{\text{sfc}}}^0 q dp, \quad (1)$$

where p_{sfc} (hPa) is the surface pressure and $g = 9.81 \text{ m s}^{-2}$ the gravitational acceleration. The convective available potential energy (CAPE; J kg^{-1} ; Emanuel 1994) is a common measure of convective instability:

$$\text{CAPE} = \frac{1}{g} \int_{p_{\text{sfc}}}^{p_{\text{lzb}}} (\alpha_{\text{pcl}} - \alpha_{\text{env}}) dp. \quad (2)$$

Here, α_{pcl} and α_{env} ($\text{m}^3 \text{ kg}^{-1}$) are the specific volumes of a lifted air parcel and the environmental air, respectively, and p_{lzb} (hPa) the pressure level, where the buoyancy of the parcel vanishes (lzb = level of zero buoyancy). In addition, a wind shear between the lower and midtroposphere, defined here as the difference of the 925- and 600-hPa horizontal wind vectors

$$\Delta V = |\mathbf{V}_{h,600} - \mathbf{V}_{h,925}| = \sqrt{(u_{600} - u_{925})^2 + (v_{600} - v_{925})^2} \quad (3)$$

[with u and v being the zonal and meridional wind components (m s^{-1}), respectively], favors the generation of intense organized convective systems (Trapp 2013).

Squall lines are closely related to low-level synoptic disturbances, so-called AEWs (Fink and Reiner 2003), as the AEWs establish high lower-tropospheric vertical wind shear and midlevel dryness in the northerlies ahead of the trough, as well as northward moisture transport between the trough and ridge (Cr  tat et al. 2015). Their westward propagation from eastern Africa to

the Atlantic Ocean can be seen in the midtropospheric relative vorticity ξ (s^{-1}), that is, the rotational component of the atmospheric flow.

b. Statistical analysis

Common measures to determine the performance of SRFE products in reproducing surface observations were employed in the statistical analysis. In particular we used the mean bias, root-mean-square error [RMSE = $1/n\sqrt{\sum_{i=1}^n(x_i - \bar{x})^2}$], and correlation coefficient r . The significance of r has been tested using a two-sided Student's t test with degrees of freedom being $N - 1$, where N is the number of data pairs. In addition, the probability that an extreme rainfall value is exceeded was estimated and expressed in terms of its return frequencies or return values (RVs) R_T defined as the value exceeded only once in a given return period T . Hence, R_T is the $1 - 1/T$ empirical percentile of the data time series.

The rather short time span of satellite data does not suffice to directly determine the return periods of extreme precipitation events with return frequencies of 100 years or more, but it is limited to the length of the time series. To estimate the probability of severe rainfall events beyond these limits, statistical distributions can be used. They describe the probability that a specific value x is exceeded and thus converge to zero for extreme values. The parameters specifying the shape of the distribution are estimated by fitting it to a set of observations and are then used to calculate the probability of any chosen value.

Gamma and Weibull distributions are two examples often used to describe rainfall intensity distributions. They are able to reproduce the main characteristics of an empirical distribution, but often fail for the most extreme values (e.g., Li et al. 2013). In this study, we therefore use the generalized Pareto distribution (GPD; e.g., Hosking and Wallis 1987), a continuous "peak over threshold" probability distribution that solely describes values exceeding a certain threshold ξ , such that the accuracy in reproducing the most extreme values is improved. The threshold value ξ is therefore critical for the accuracy of the distribution.

The GPD can be expressed by the quantile function, that is, the inverse of the probability density function (PDF),

$$x(F) = \begin{cases} \xi + \alpha \times \frac{1 - (1 - F)^\kappa}{\kappa}, & \kappa \neq 0 \\ \xi - \alpha \times \log(1 - F), & \kappa = 0 \end{cases}, \quad (4)$$

where F is the percentile; x is the resulting quantile; and κ , α , and ξ are the shape, scale, and location parameters

of the distribution, respectively. If both κ and ξ are zero, the GPD is equivalent to the exponential distribution. Note that there are different sign conventions in the literature for the shape parameter κ .

To estimate the parameters of the GPD, the L-moments λ_i of the ordered sample $X_{1:n}$ of size n are calculated according to Hosking (1996). Following Paeth and Hense (2005), only rainfall events above 1 mm within 24 h are considered. Then, extreme events are selected by using values above the 80th percentile, which defines the lower limit ξ of the GPD. The uncertainty of the distribution can be determined with a bootstrapping technique (Paeth and Hense 2005): N samples of size M that are randomly selected from the fitted GPD and used to create a new fit. The standard deviation σ of the resulting set of fits is a measure of uncertainty of the GPD. For this study, $N = 50$ samples with $M = 1000$ values used.

4. Dynamical analysis

Two cases of extreme precipitation in West African cities are discussed in this paper. Both were the highest precipitation values within 24 h that the respective stations recorded since the beginning of operation in the early twentieth century. The events occurred during the peak of the rainy season, and their exceptionally high rainfall amounts led to severe floods with thousands of inhabitants affected and several casualties.

a. Case 1: Ouagadougou, Burkina Faso, 1 September 2009

At 0600 UTC 2 September 2009, the synoptic weather station at the international airport of Ouagadougou, the capital of Burkina Faso with about 1.5 million inhabitants (UNDP 2015), reported an accumulated precipitation amount of 261.3 mm for the previous 24 h, that is, more than the mean monthly precipitation of August, the wettest month of the rainy season. In fact, about one-third of the mean annual sum fell on a single day. This value was the highest ever recorded at this station and exceeds the second-largest value by nearly 100 mm day⁻¹, that is, a factor of 1.6. Figure S1 in the online supplement shows that a second station to the south reported 212.8 mm, and three other stations measured well above 100 mm. Data from the station network indicate that an area of nearly 10 000 km² may have received on the order of 100 mm or more, suggesting that the extreme event affected several 25 km × 25 km TRMM 3B42 and PERSIANN-CDR pixels. According to half-hourly airport METAR reports, the convective system causing this rainfall passed over the city on 1 September 2009 between 0600 and

1700 UTC, with the heaviest rain rates between 0600 and 1200 UTC. This is corroborated by the 1200 UTC synoptic station (SYNOP) report at Ouagadougou giving a 6-h total of 237 mm during this period. Usually the morning hours are quite unfavorable for MCS genesis due to low convective instability (Fink and Reiner 2003). Thus, the questions arise as to what type the convective system was and what may have caused its extreme strength during an unfavorable period of the diurnal cycle.

Figure 2 shows brightness temperatures from the 150-GHz channel of the Advanced Microwave Sounding Unit B (AMSU-B) [157-GHz channel of the Microwave Humidity Sounder (MHS) in Fig. 2c] from all (irregular) overpasses between 31 August and 1 September 2009. Microwave window channels reliably delineate deep continental convection in contrast to infrared brightness temperatures, for which cirrus anvils conceal convectively active regions (Redl et al. 2015). A linear, squall line-type system with two main convective regions is located over southwestern Niger in the evening of 31 August (Fig. 2a). Convection enters eastern Burkina Faso around midnight (Figs. 2b,c) and reintensifies in the morning, when it arrives at Ouagadougou from the east (Fig. 2d). By 0152 UTC 1 September, the northern cell is decaying, while the southern one has grown into a large oval-shaped convective region. The two early morning overpasses at 0503 and 0613 UTC (Figs. 2d,e) show a very unusual development: the convection develops a very strong curvature at its southern flank, and a second intense cell forms behind the leading band of convection (located to the northeast of Ouagadougou at 0613 UTC; Fig. 2e). By 0945 UTC, the leading band has passed Ouagadougou, but intense convection continues in association with the trailing and still-developing second cell.

Animation A1 in the online supplement to this article impressively shows the temporal evolution of the system described above with 15-min infrared scans from the Spinning Enhanced Visible and Infrared Imager (SEVIRI) aboard MeteoSat Second Generation (MSG; Schmetz et al. 2002). Several convective cells occur in the northwest of Nigeria on 31 August and merge to a single system. Even the rotation can be clearly seen when the system passes over Burkina Faso. After reaching Ouagadougou in the morning of 1 September, the huge cloud shield suddenly dissolves, and the system is accelerated to the west. From this satellite analysis, it can be concluded that the MCS was not a linear squall type system, but showed signs of rotation of convective cells. More importantly, this went along with cells developing behind the leading band, and Ouagadougou was affected by at least two intense convective cells within 6 h (cf. Figs. 2d–f).

Different types of convection are generally associated with different vertical wind profiles (Lafore et al. 2017). Typical squall line environments in West Africa show an abrupt jump from low-level southwesterlies to midlevel easterlies, resulting in a rather linear hodograph. In stark contrast, the hodograph for 0600 UTC 1 September 2009 at the ERA-I grid point closest to Ouagadougou (Fig. 3) shows strong and deep tropospheric speed and directional vertical shear. The winds rotate at low levels, which is reminiscent of situations in which supercells with rotating updrafts occur in subtropical and midlatitude convective outbreaks. Because of the absence of ground-based radar monitoring, it remains unclear if MCSs with rotating updrafts were present, but Lafore et al. (2017) mention the potential occurrence of supercells at the flanks of West African squall lines. In any case, reasons for the highly unusual directional shear and curving of convection described above warrant further inquiry.

Synoptic-scale midtropospheric cyclonic rotation in winds over West Africa is often associated with troughs of AEWs. Figure 4a depicts vectors of vertically integrated humidity flux at 0600 UTC 1 September that mimic the flow in the lower troposphere, where more than 80% of the total moisture is found. A strong cyclonic vortex centered over northern Benin is evident. Moisture is advected cyclonically around the trough, and extreme moisture convergence of more than $1.4 \times 10^{-3} \text{ kg m}^{-2} \text{ s}^{-1}$ ($= 121 \text{ mm day}^{-1}$) is found in the center of the vortex (red contours in Fig. 4a). This leads to very high values of TPW above 60 kg m^{-2} , exceeding the 99th percentile of TPW for the entire 1979–2014 period (gray shading in Fig. 4a) in the area of the trough and to its northwest, already including the Ouagadougou area (yellow star in Fig. 4a). Large parts of this system even show the highest TPW values of the entire ERA-I period. The cyclonic vortex is part of a distinct AEW ridge–trough system, the former being located over Guinea and Sierra Leone. To the west of the trough, the 0600 UTC analysis shows enhanced lower-tropospheric wind shear of $10\text{--}20 \text{ m s}^{-1}$ over northern Burkina Faso and westernmost Niger, but because of the early morning hours, CAPE is lower than 1000 J kg^{-1} (Fig. 4b). From this, we conclude that the convective invigoration must be related to synoptic forcing from the AEW that provided strong convergence and record amounts of moisture. Canonical squall lines deplete the atmosphere of moisture, and the rear flow is usually subsiding and dry (Lafore et al. 2017). Figure 4a suggests that the circulation in the vortex may have contributed to a swift moisture recharge that allowed the unusual development of a second cell behind the main leading edge to form (cf. Fig. 2e).

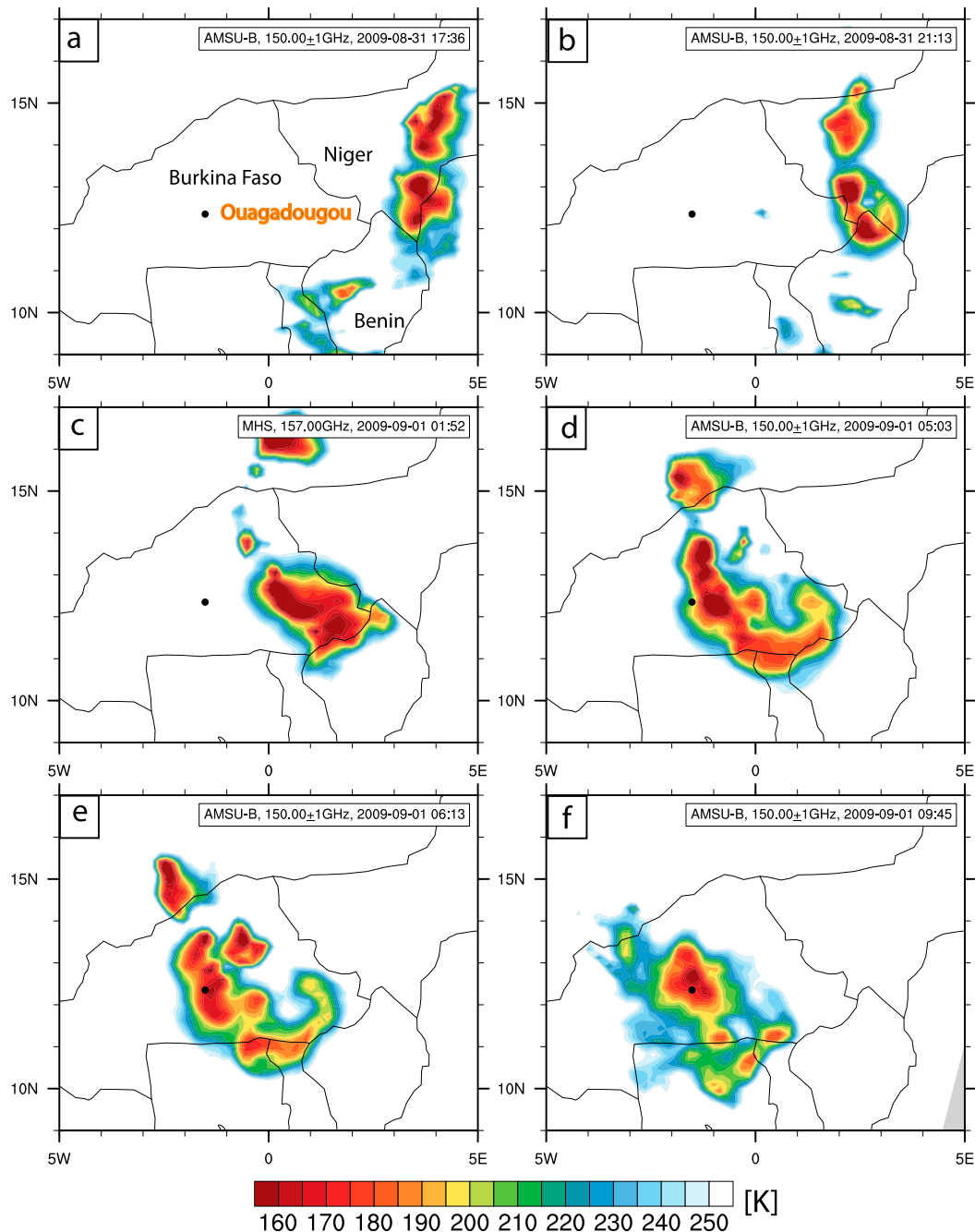


FIG. 2. Time evolution of the convection causing the Ouagadougou flood. Shown are brightness temperatures (K) in the swaths from all overpasses between 1700 UTC 31 Aug and 1000 UTC 1 Sep 2009. Exact overpass times are (a) 1736, (b) 2113, (c) 0152, (d) 0503, (e) 0613, and (f) 0945 UTC. Imagery from the 150-GHz channel of the AMSU-B is used in (a), (b), and (d)–(f), and the 157-GHz channel of the MHS is shown in (c). The location of Ouagadougou is marked with a black dot, and some place names are indicated in (a).

The east–west propagation of AEWs is best analyzed from Hovmöller diagrams of meridionally averaged (5° – 15° N) relative vorticity at 700 hPa. Figure 5 shows a succession of two very strong AEW vortices at the end of August and in the first days of September 2009. The first

AEW crosses Ouagadougou around 30 August. Apart from high values of relative vorticity, the first AEW slowed down to about half of the typical AEW propagation speed of 6 – 8 m s^{-1} just downstream of Ouagadougou (gray numbers in Fig. 5). This may have enhanced tropospheric

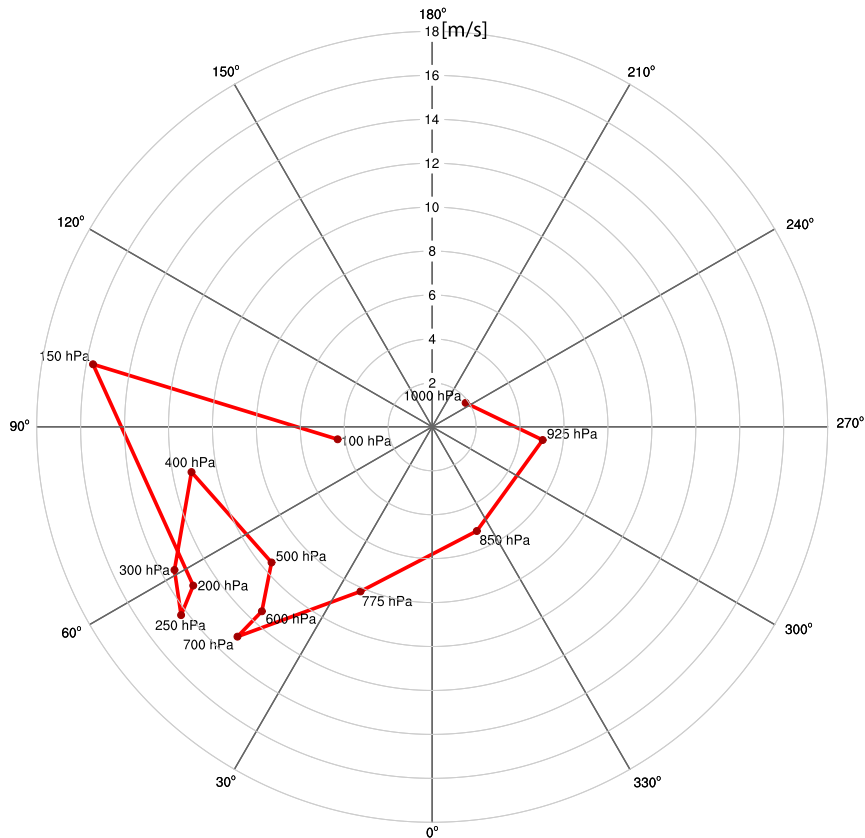


FIG. 3. Vertical wind profile during the Ouagadougou flood event as seen in a hodograph, constructed from ERA-I winds at the grid point closest to Ouagadougou for 0600 UTC 1 Sep 2009. Wind direction ($^{\circ}$; according to a standard meteorological wind rose) and speed (m s^{-1}) are plotted in a polar diagram, and the points at the different pressure levels from 1000 to 100 hPa are connected by a red line.

moisture content in the southerlies behind the trough. The second AEW is at about 4°E at 0000 UTC 1 September (as also discussed in Galvin 2010). At this longitude, it slows down to a propagation speed of 3.8 m s^{-1} and 700-hPa relative vorticity reaches up to $4.8 \times 10^{-5} \text{ s}^{-1}$ (Fig. 5). This value is averaged over the 5° – 15°N latitude band. At 850 hPa, relative vorticity at the T106 spectral resolution is greater than $1.5 \times 10^{-4} \text{ s}^{-1}$ over southwestern Niger at 0600 UTC 1 September 2009 (Fig. 6). In this region, the 99.9th percentile is exceeded (Fig. 6), and several grid points showed their highest value observed for the period 1979–2014. Similar extreme values were observed at the other analysis times on 1 September 2009, that is, at 0000, 1200, and 1800 UTC. The second AEW is also unusually deep with positive vorticity values up to 450 hPa (not shown). Consistent with the satellite animation (see Animation A1 in the online supplement), the AEW-related vorticity maximum decreases considerably over and downstream of Ouagadougou and accelerates to 19 m s^{-1} , suggesting a collapse of the convection and the vortex. These are tightly connected, as convection in the AEW

trough is an important source of relative vorticity over West Africa (e.g., Fortune 1980). Thus, part of the strong rotation is related to the strong convection itself. In summary, two very strong AEWs and their atypical slow propagation behavior provided record-breaking tropospheric moisture contents, allowed the convection to reinforce in the second half of the night and morning hours, turned the convective band counterclockwise at its southern end, and finally allowed a second strong cell to develop and pass over Ouagadougou.

b. Case 2: Dakar, Senegal, 26 August 2012

On 26 August 2012, the weather station at the airport at Dakar-Yoff reported a rainfall total of 160.8 mm. This was the highest recorded value ever at this station,¹ although at least two events showed a similar magnitude

¹ In 1932, the station Dakar L'Hôpital recorded a 24-h accumulation of 212 mm; no information on the correctness of this value was found.

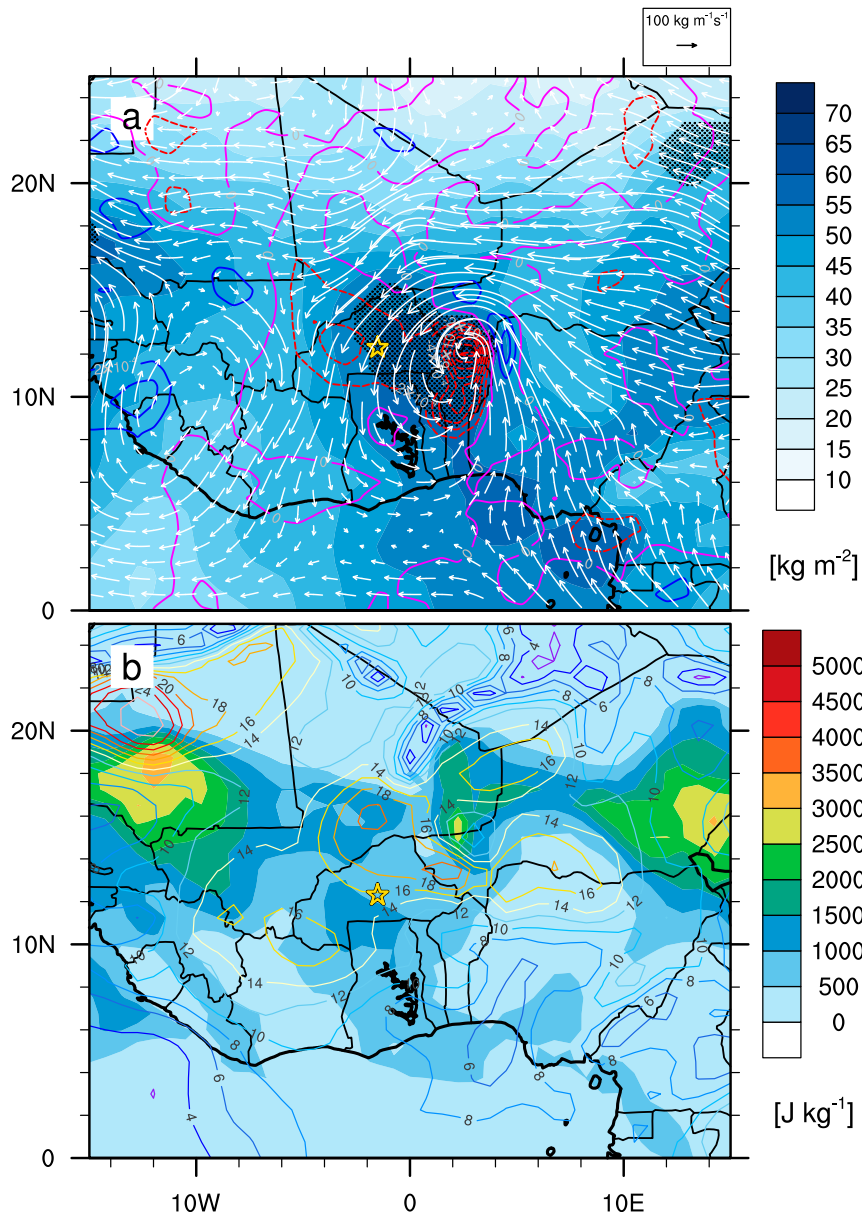


FIG. 4. Synoptic situation leading to the Ouagadougou flood event. (a) TPW (shading; kg m^{-2}), humidity flux (vectors; $\text{kg m}^{-1} \text{s}^{-1}$), and humidity flux divergence (contours; $\text{kg m}^{-2} \text{s}^{-1}$) and (b) CAPE (shading; J kg^{-1}) and shear velocity between 925 and 600 hPa (contours; m s^{-1}) for 0600 UTC 1 Sep 2009 from ERA-I reanalysis. The stippled areas in (a) show where TPW exceeds the 99th percentile (1979–2014). The yellow star shows the location of Ouagadougou.

(157.7 mm day^{-1} on 25 August 1964 and 153.1 mm day^{-1} on 26 August 1962). Widespread flooding within the city of Dakar occurred on this day, with 287 000 residents being displaced and 18 deaths, motivating the Senegalese government to declare a state of emergency (Cornforth 2013).

According to SYNOP and METAR observations from Dakar-Yoff, there were two periods of thunderstorm activity for the 24-h period starting at 0600 UTC

26 August. The first one occurred between 0900 and 1400 UTC, producing most of the observed daily rainfall total. According to the SYNOP and METAR reports, 161 mm fell within just 6 h between 0600 and 1200 UTC. The amount of rain in the 51 min between 0946 and 1036 UTC was 144 mm, with a peak 1-min intensity of 420 mm h^{-1} (A. Diongue Niang, ANACIM, 2015, personal communication). Further convective cells appearing in the evening between 2000 and 2230

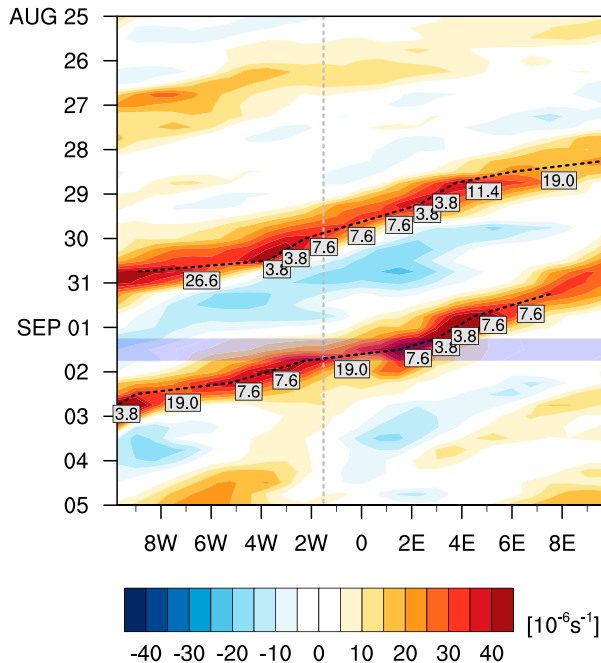


FIG. 5. AEW development associated with the Ouagadougou flood event. Hovmöller diagram of relative vorticity (10^{-6} s^{-1}) at 700 hPa from ERA-I reanalysis, averaged over 5° – 15° N, for the time period from 25 Aug to 5 Sep 2009. The dashed black lines show the position of the maximal vorticity, and the numbers show the propagation velocity (m s^{-1}). The gray line marks the longitudinal position of Ouagadougou, and the blue shaded box marks the time period of heavy rainfall.

UTC seem to have only produced traces of rainfall at Dakar-Yoff. The rainfall distribution in the course of 26 August 2012 differed from the climatological diurnal cycle of precipitation over Dakar, as analyzed by Sane et al. (2012), who found a dominant peak at 1500–1700 UTC and a second one at 0900–1100 UTC with lower rain rates. Figure 7 shows the evolution of the thunderstorm over Dakar with the AMSU-B and MHS measurements. A mostly south–north-oriented band with several cells of low brightness temperatures reaches Dakar in the early morning (Fig. 7a). The intense northernmost convective maximum passed directly over the city between about 0800 and 1200 UTC (Figs. 7b–d) and then dissolves (Fig. 7e).

The vertically integrated flux of humidity at 1200 UTC 26 August 2012, obtained from ERA-I, is depicted in Fig. 8a. It shows a strong westward transport from the Sahel to the east of an AEW trough that crossed Senegal the day before. Extreme moisture convergence occurs at the coast of Guinea, but there is no noteworthy convergence visible over Dakar. Though TPW reaches up to 60 kg m^{-2} over the Dakar area, exceptionally high atmospheric moisture contents above the 99th percentile are confined to the convergence center over Guinea and

to the southwest of Dakar over the Atlantic Ocean. A highly unstable atmosphere with CAPE values exceeding 5000 J kg^{-1} , as well as a moderate wind shear ($\leq 15 \text{ m s}^{-1}$; Fig. 8b) to the east of the city, favor the generation of severe thunderstorms, although such conditions are not very unusual in this area. Similar to the Ouagadougou case, the AEW trough passage led to a nighttime enhancement of convection and excessive rains associated with a slow-moving, multiple-cell MCS in a very moist atmosphere. Visual inspection of satellite animations (see online supplemental material, Animation A2) and the fact that the development took place around the secondary early morning rainfall peak (Sane et al. 2012) suggest that the land–sea breeze in the Cape Verde area contributed to the enhancement of convection and recurrent new cell generation. However, although the rain event was the most severe at the Dakar-Yoff station, its physical causes appear to be a coincidental combination of effects that are each frequently observable there.

5. Statistical analysis

Using the two cases discussed in section 4 as illustration, here we examine the capability of SRFE to reproduce observed rain rates and their applicability for a flood risk assessment for the African continent. For this, the satellite data will be directly compared to the surface measurements to highlight systematic differences between these two sources of rainfall information.

a. Comparison of satellite to gauge data

Generally speaking, a quantitative point-to-pixel analysis of daily rainfall is fraught with problems, particularly in areas affected by isolated thunderstorms. As both Dakar and Ouagadougou are climatologically dominated by large MCS-related rainfall, such a comparison should be more robust than in many other locations in Africa. Figure 9 shows scatterplots of the nearest pixel in TRMM 3B42 (Figs. 9a,b) and PERSIANN-CDR (Figs. 9c,d) against gauge data from the synoptic stations Ouagadougou Aéro (Figs. 9a,c) and Dakar-Yoff (Figs. 9b,d), including linear regression lines and correlation coefficients. To better illustrate the differences of these datasets, only rain rates above 1 mm day^{-1} are considered, and the overlapping time period from 1998 to 2014 is used. Both satellite products show substantial deviations from the gauge data on a daily basis, resulting in a broad scatter around the unity line. PERSIANN-CDR and TRMM show similarly low, but significant (at the 99% level), correlations (0.32 and 0.25 for Ouagadougou and 0.49 and 0.34 for Dakar, respectively), revealing a limited ability

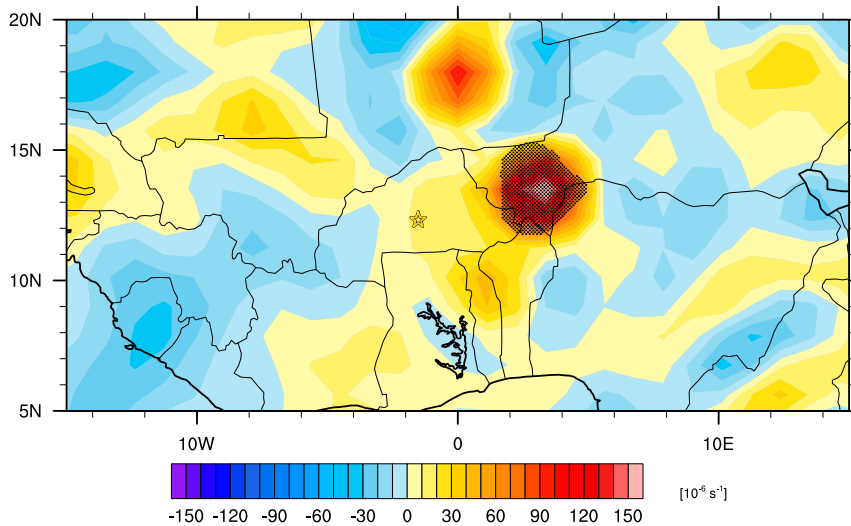


FIG. 6. Exceptionality of the second AEW for the Ouagadougou case. Shown is the relative vorticity at 850 hPa at 0600 UTC 1 Sep 2009, with areas exceeding the 99.9th percentile stippled. A spectral resolution of T106 is used here to smooth the often noisy vorticity field stressing the synoptic-scale nature of AEWs.

to reproduce daily time series at a certain location. A small increase in correlation for PERSIANN-CDR seems possible if the accumulation period would have been from 0600 to 0600 UTC instead of from 0000 to 0000 UTC, but because of its temporal resolution, we were not able to test this directly.

However, several tests with longer accumulation periods and larger areas with more stations were carried out. Figure 9 was reproduced using 48- and 72-h accumulation periods, reducing the nonoverlapping time period for PERSIANN-CDR from 25% to 13% and 8%, respectively (not shown). The stronger negative bias and generally lower correlation coefficients of PERSIANN-CDR are robust for these longer periods. Another test was carried out by adding a second available station to the $0.25^\circ \times 0.25^\circ$ latitude–longitude square in which the Ouagadougou station is located (region 3 in Fig. 1b), and by repeating this analysis for $0.5^\circ \times 0.5^\circ$ and $1^\circ \times 1^\circ$ latitude–longitude rectangles that contain three and seven stations for the TRMM and three and nine stations for the PERSIANN-CDR period, respectively (regions 1 and 2 in Fig. 1b). As expected, adding another station to region 3 increases the linear correlation, as does the consideration of larger areas with more stations, but the correlation with TRMM remains higher. The correlation differences even increase with the larger areas (Fig. S2). Recall, however, that any linear correlation analysis depends on phase coincidence, not amplitude. Thus, not unexpectedly, the value ranges of the two satellite products largely differ. PERSIANN-CDR is limited to rain rates of less than 80 mm day^{-1} in

Ouagadougou and slightly more than 60 mm day^{-1} in Dakar. The most intense rainfalls observed at the surface stations are considerably underestimated by PERSIANN-CDR, as seen in the flattening of the scatterplot. TRMM, on the other hand, shows values exceeding 100 mm day^{-1} for Ouagadougou. The broad scattering of TRMM results in RMSEs of 20.73 and $18.92 \text{ mm day}^{-1}$, which is larger than for PERSIANN-CDR with 17.23 and $18.01 \text{ mm day}^{-1}$, whereas the mean bias is lower (TRMM: 1.27 and 0.90 mm day^{-1} , PERSIANN-CDR: -3.24 and $-3.34 \text{ mm day}^{-1}$). The slopes of the regression lines are less than 1 in all panels of Fig. 9, indicating a systematic underestimation of the observed rain rates, with PERSIANN-CDR showing an even flatter slope than TRMM. For Ouagadougou (Dakar), TRMM has a slope of 0.33 (0.49) and PERSIANN-CDR 0.13 (0.20). These findings are robust for adding a station to region 3 and for the larger regions 1 and 2 with more stations, except for a smaller bias of PERSIANN-CDR in the largest region 1 (Fig. S2)

The examined flood cases are encircled in Fig. 9. Both TRMM and PERSIANN-CDR strongly underestimate the rain rate for the Ouagadougou flood case. TRMM only estimates about 70 mm for the Ouagadougou case. For the Dakar case, 120 mm is reasonable and is the most extreme value in the TRMM period (Fig. 9b). Underestimation in PERSIANN-CDR data is a factor of 6 in the Ouagadougou case and a factor of more than 2 for Dakar.

A common problem of point-to-pixel comparisons is that, due to small-scale convective systems, the gauge

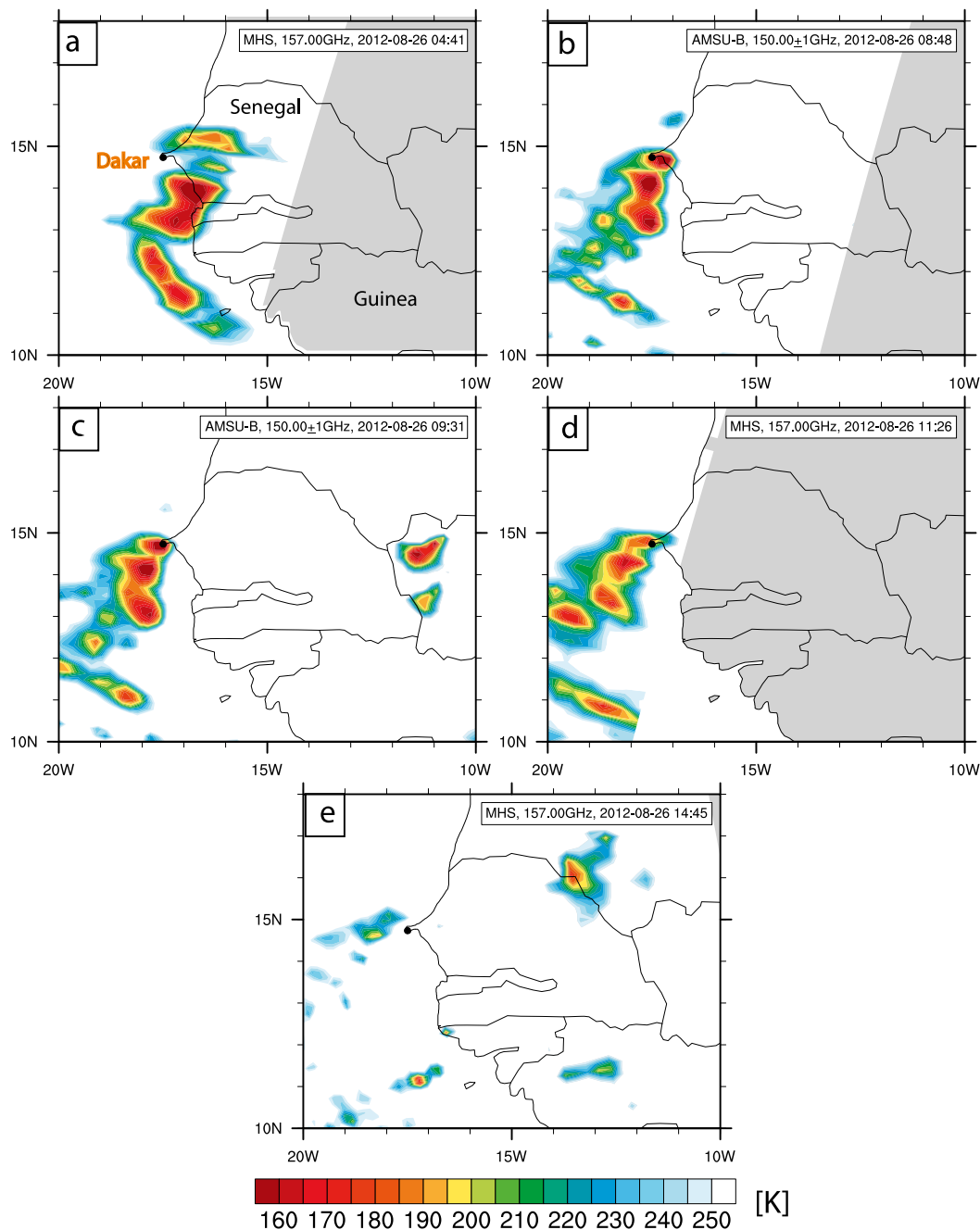


FIG. 7. As in Fig. 2, but for the Dakar flood case, 0400–1500 UTC 26 Aug 2012. Exact timings and satellite instruments are given in each panel.

data reports no precipitation, while the spatially aggregating satellite data have a nonzero value. However, the satellite should detect rainfall when the surface station credibly reports it. Hence, we compare the percentage of matching zero/nonzero values between the gauge and satellite data for 1998–2014 in Fig. 10. The majority of days show no rainfall for both station and satellite, but TRMM has a larger fraction than PERSIANN-CDR

(74.6% for Ouagadougou and 82.3% for Dakar compared to 56.7% and 69.6%, respectively). PERSIANN-CDR reports rainfall much more often than observed at the station gauge (24.4% and 19.5% versus 6.6% and 6.8% for TRMM, respectively; gray boxes in Fig. 10). This can generally be understood by localized convective events within the satellite pixel not affecting the station, making part of this disagreement physically

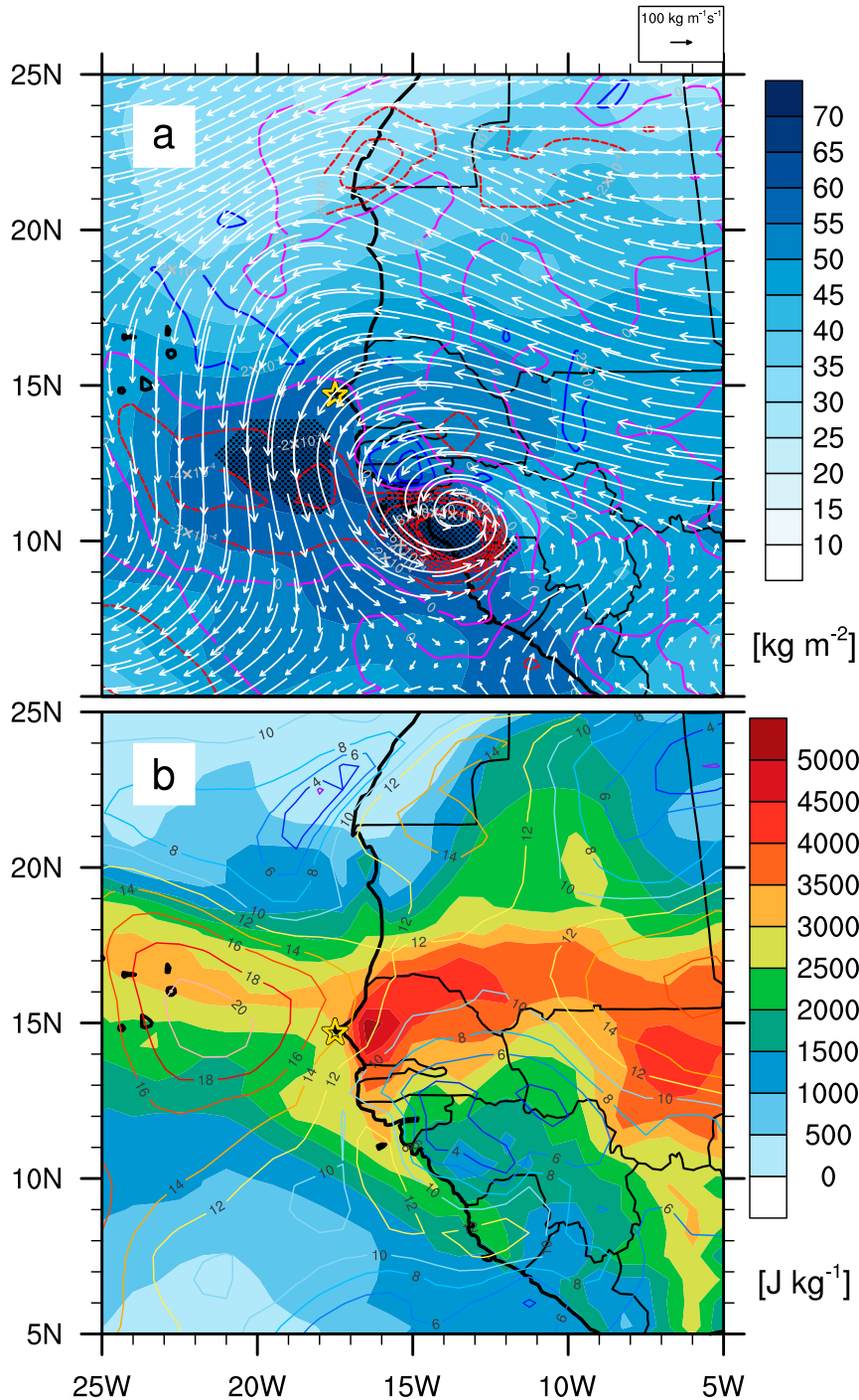


FIG. 8. As in Fig. 4, but for the Dakar flood case showing 1200 UTC 26 Aug 2012. The yellow star shows the location of Dakar.

plausible. However, the large difference between the two products suggests that PERSIANN-CDR erroneously flags cold, nonprecipitating cirrus anvils as rainy, giving true “false alarms.” In line with this, TRMM has a higher fraction of events, for which the station reports

rainfall, but the satellite does not (red boxes in Fig. 10). These are not physically plausible and are therefore true “missed events.” Given the overall much higher fraction of rain in PERSIANN-CDR (40.8% for Ouagadougou and 29.2% for Dakar versus 19.0% and 15.9% for

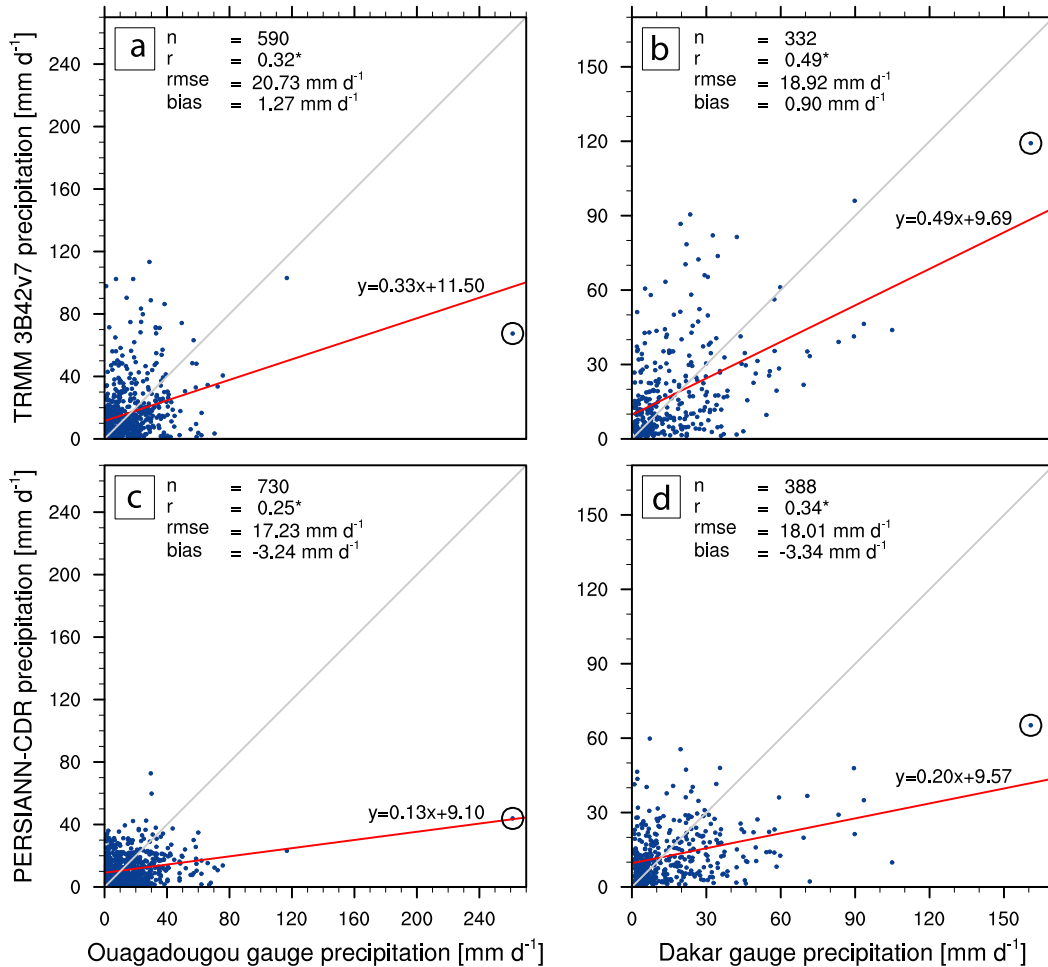


FIG. 9. Point-to-pixel comparison between station data and SRFEs. Scatterplots of daily (top) TRMM 3B42 (0600–0600 UTC) and (bottom) PERSIANN-CDR (0000–0000 UTC) precipitation estimates against daily gauge data (0600–0600 UTC) at (a),(c) Ouagadougou Aéro (ID: 65503) and (b),(d) Dakar-Yoff (ID: 61641) for 1998–2014. The encircled values show the analyzed cases. Only rain pairs with rain rates of more than 1 mm day⁻¹ are considered explaining the different sample sizes.

TRMM), rates of hits are also higher, probably at the cost of many false alarms. The total proportion correct, that is, the sum of the correct negative and hits in the diagonal of the contingency table, is higher for TRMM than for PERSIANN-CDR (87% for Ouagadougou and 86.1% for Dakar versus 73.1% and 70.8%). A fairer comparison taking into account the chance of random correct forecasts is the Heidke skill score (HSS), suggesting a much better performance of TRMM (0.58) than PERSIANN-CDR (0.39, Table 1). In the online supplement to this article, we repeat this exercise for Ouagadougou with more stations and larger pixels (see main results in Table 1 and Fig. S3). Considering the same satellite pixel but including information from a second station expectedly improves all scores, increasing HSS values to 0.7 and 0.45, respectively. Interestingly, the number of false alarms is only mildly reduced, suggesting that rainfall from isolated

showers is rather infrequent. In the continental Sahel, about 90% of the rainfall comes from MCSs (Mathon et al. 2002) with rainfall areas in excess of 10 000 km², much larger than the satellite pixels. Moving to pixel sizes of 0.5° and 1.0° with three and seven stations for TRMM (three and nine for PERSIANN-CDR), respectively, increases the number of hits at the expense of correct negatives, but somewhat reduces the proportion correct and HSS in most cases (Table 1). This suggests that more stations would be needed to match the result of the smaller pixels with two stations. The fundamental differences between the two satellite datasets are robust.

b. Return values

In the previous subsection, it was shown that TRMM provides better estimates of extreme daily rainfall despite the dramatic underestimation of the Ouagadougou

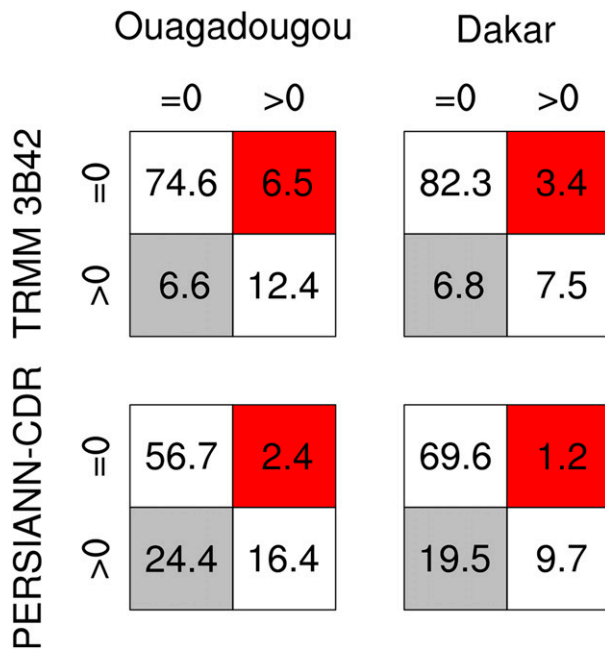


FIG. 10. Evaluation of rainfall frequency. Contingency tables showing percentages of (dis)agreement between rainfall occurrence at (left) Ouagadougou and (right) Dakar-Yoff from gauge data when compared with SRFEs from (top) TRMM 3B42 and (bottom) PERSIANN-CDR. Fields with rainfall in the satellite estimates but not observed at the station are shaded in gray, and the opposite situation is in red.

event. Here, we analyze the implications of this for RVs of extreme precipitation derived from the two SRFEs and the centennial gauge time series. Figure 11 shows the empirical and statistically fitted RVs as well as their uncertainty range as a function of their return frequency for Ouagadougou (Fig. 11a) and Dakar (Fig. 11b). The fitting has been applied to the whole available time period of gauge data, and the nearest pixel from TRMM and PERSIANN-CDR, respectively (see section 2 for details on data availability).

For frequencies up to about 40 years, the GPD fit of the gauge data in Ouagadougou is in good agreement with the empirical values (Fig. 11a). A return frequency of 100 years shows RVs of $145 \pm 42 \text{ mm day}^{-1}$. However, the most extreme value of $261.3 \text{ mm day}^{-1}$, which has an empirical return frequency of 113 years (i.e., the length of the station time series), is nearly twice the estimated value from the GPD and outside of the uncertainty limits. Using the GPD fitted to gauge data, this event has a return frequency of about 14 000 years. This underlines the exceptionality of this event that could not have been anticipated even from a gauge time series of more than 100 years. Other methods of estimating the GPD (variation of the precipitation quantile, estimation of ξ , and other algorithms to estimate the GPD parameters) give similar results (not shown).

The GPD fit of TRMM 3B42 shows centennial RVs of $155 \pm 55 \text{ mm day}^{-1}$. In contrast, PERSIANN-CDR drastically underestimates the observed return values, consistent with Fig. 9. Precipitation amounts of $59 \pm 17 \text{ mm day}^{-1}$ are expected to occur once in 100 years. Such values would hardly have any socioeconomic impacts, and thus an analysis relying on PERSIANN-CDR alone would cause a misjudgment of the flood risk. The uncertainty range is quite low, suggesting a high reliability of the statistical fitting, but the two heaviest precipitation events of PERSIANN-CDR are slightly outside of this range (green dashed line in Fig. 11a). This means that, in addition to the systematic underestimation of RVs with PERSIANN-CDR, the most extreme situations are underestimated even more strongly. These notions also hold for the smallest region 3 with two stations and the larger regions 1 and 2 (Fig. S4).

For Dakar, the fit of gauge data matches the observed empirical RVs well (Fig. 11b). The heaviest events are slightly overestimated but are within the uncertainty range. An RV of $192 \pm 55 \text{ mm day}^{-1}$ is estimated for a 100-yr return period. The uncertainty range is higher than in Ouagadougou because of fewer events with at least 1 mm precipitation. TRMM shows a good agreement for return periods below 10 years and a slight underestimation of more rare events. A value of $157 \pm 34 \text{ mm day}^{-1}$ is expected once in a century. PERSIANN-CDR again suffers from its limited value range, showing only $88 \pm 22 \text{ mm day}^{-1}$ for a return frequency of 100 years. In summary, the RV analysis suggests that TRMM SRFE might be suitable to estimate centennial RVs using the peak-over-threshold approach with a GPD fit, whereas PERSIANN-CDR is less suitable for this purpose, despite having an observational period that is twice as long. However, the Ouagadougou event shows that highly unusual dynamical developments can create extreme situations well outside of any RV estimates.

6. Summary and conclusions

Two recent extreme flooding events in large urban agglomerations in the West African Sahel were investigated: the 1 September 2009 flood in Ouagadougou (Burkina Faso) and the 26 August 2012 flood in Dakar (Senegal). In both cases, the largest 24-h rainfall accumulations in the respective 100-yr time series were observed. The events were analyzed in terms of the dynamic causes using satellite and ERA-I data, and with respect to their statistical exceptionality using the long gauge time series and two satellite-based daily rainfall estimates, PERSIANN-CDR (1983–2014) and TRMM 3B42 V7 (1998–2014).

TABLE 1. Summary of results for satellite–station precipitation comparisons for the areas of Dakar and Ouagadougou. The third column gives the satellite pixel size and the number of stations in this pixel, the fourth column gives the region number 1–3 (see Fig. 1b), B = frequency bias, and PC = proportion correct. The full contingency tables are given in Figs. 10 and S3.

Location	Dataset	Pixel size/No. of stations	Region No.	B	PC (%)	HSS
Ouagadougou	TRMM	0.25°/1	3	1.0	87.0	0.58
		0.25°/2	3	0.9	90.4	0.70
		0.50°/3	2	1.2	88.4	0.69
		1.00°/7	1	1.1	84.5	0.65
	PERSIANN-CDR	0.25°/1	1	2.2	73.1	0.39
		0.25°/2	1	2.0	75.9	0.45
		0.50°/3	2	2.2	70.8	0.40
Dakar	TRMM	0.25°/1	—	1.3	89.8	0.54
		0.25°/1	—	2.7	79.3	0.39

In terms of its synoptic–convective dynamics, the Ouagadougou case is truly exceptional. A succession of two strong and slow-moving AEWs (the second arguably the strongest AEW in the 1974–2014 period) caused excessive values of tropospheric moisture and provided the synoptic forcing for the nighttime genesis of MCSs. Cornforth et al. (2017) ascribe the slow propagation of the AEW to a wave breaking event. The abovementioned MCSs were not of the fast-moving, squall line type typically associated with AEW troughs (Fink and Reiner 2003) and yielding daily accumulations in the 20–50 mm range (Fink et al. 2017). Instead, the convective bands were curved cyclonically at the southern flank of the active area due to the very strong low- to midtropospheric

AEW vortex. As a consequence, Ouagadougou was hit by two MCSs within 6 h, the latter being possible because of the rotation and swift moisture refueling by the strong convergence in the AEW-related vortex. An ERA-I derived hodograph showed deep tropospheric wind shear susceptible to the formation of a supercell with rotating updrafts. Galvin (2010) describes the role of the second wave trough in forcing the Ouagadougou convective event and in providing moisture at its eastern flank. He did not refer to the strong rotation and its potential role in generating the second convective cell hitting Ouagadougou. In fact, to the best of our knowledge, such a strongly rotating AEW in combination with an MCS in Africa has never been mentioned in the literature before.

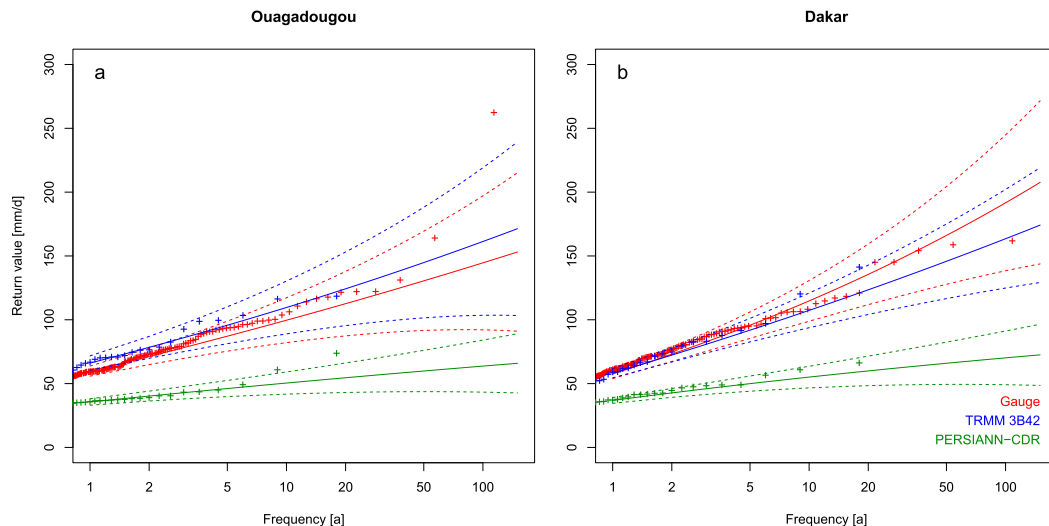


FIG. 11. Estimation of RVs for daily precipitation. Empirical (plus signs) and fitted (solid lines) RVs (mm day^{-1}) for (a) Ouagadougou and (b) Dakar–Yoff from 0600–0600 UTC gauge data (red), 0600–0600 UTC TRMM 3B42 (blue), and 0000–0000 UTC PERSIANN-CDR (green) as a function of their return frequency (in years). The dashed lines indicate the uncertainty range of the fits. Note that the sample used to infer RVs is not identical to Fig. 9 since in this figure the longest available time series were taken per data source (cf. sections 2a and 2c).

The Dakar case was similar in that the tropospheric environment was very moist and that a nighttime AEW trough passage forced convection to the east. Here, however, the longevity of the convection might be related to moisture feeding by the land–sea breeze in combination with a restoring of high CAPE values through advection from the east. The dynamic analysis suggests that the synoptic environment in this case was not as unusual as in the Ouagadougou case.

The Ouagadougou 24-h rainfall accumulation exceeded the previous highest observed gauge value by nearly 100 mm, underpinning its extreme nature. Analysis of empirical and statistical RVs from 100-yr-long daily gauge data, PERSIANN-CDR and TRMM also underline this. Using the gauge data, the event was well outside the estimated uncertainty limits at the extreme end of the distribution. Our analysis also shows that TRMM appears to be better suited than PERSIANN-CDR to assess flood risks despite being almost twice as long as the 17-yr TRMM dataset. Centennial RVs were much higher for TRMM, and in the Ouagadougou case, the RVs were in the range of the value that was statistically estimated using the 113-yr-long daily gauge series. Despite this encouraging result for TRMM, some caveats remain that require further study. Over Africa, ice water particles in cumulonimbus clouds are unusually large and soils in the Sahel have a low emissivity at microwave wavelengths, both leading to overestimation of rainfall rates by passive microwave algorithms (Liu et al. 2008; Liu and Zipser 2014). Moreover, rainfall rates are overestimated at infrared wavelengths due to nonraining cirrus anvils. Thus, it cannot be excluded that the high return values of TRMM are an artifact of the algorithm. The strong underestimation of the Ouagadougou event supports the idea of possibly getting a right answer for a wrong reason. For this region, eight other rain gauges were available, and our inferences were overall robust against tests with more rain gauges and larger regions. Yet, the number of rain gauges in the larger $0.5^\circ \times 0.5^\circ$ and $1^\circ \times 1^\circ$ latitude–longitude squares around Ouagadougou was still too low for a rigorous assessment of the TRMM 3B42 and PERSIANN-CDR performance. Mesonetworks with about 30–50 rain gauges providing hourly data have been maintained by the Analyse Multidisciplinaire de la Mousson Africaine–Couplage de l'Atmosphère Tropicale et du Cycle Hydrologique (AMMA-CATCH) initiative (<http://www.amma-catch.org/?lang=fr>) in the Niamey area and in central Benin now for three and two decades, respectively; using these data, an exact overlap of 24-h periods with PERSIANN-CDR could be obtained and more pixels with more than one rain gauge could be considered. Such a thorough

study should ideally involve comparisons with other gauge-calibrated, daily satellite products.

The present study adds new insights to a quite limited body of work on the recurring threat of urban flash flooding in Africa due to extreme rainfall (Tarhule 2005; Tschakert et al. 2010). West Africa has seen a number of floods in rainy seasons (Paeth et al. 2011; Njau and Thiaw 2011; Sima et al. 2013) in recent years and a significant increase in daily rainfall above the 95th percentile (Sanogo et al. 2015). Whether the associated overall rainfall recovery in the Sahel is related to natural decadal variations in the tropical oceans or greenhouse gas–related warming is under debate (Rodríguez-Fonseca et al. 2011; Dong and Sutton 2015). Hirabayashi et al. (2013) indicate that higher atmospheric moisture as a consequence of global warming might increase the frequency of floods. Martin and Thorncroft (2015) found stronger AEWs in CMIP5 models at the end of this century due to an enhanced land–sea thermal contrast. Whether this would also cause stronger rainfall associated with these AEWs is unclear.

Simple arguments on future increases of extreme rainfall events involve Clausius–Clapeyron scaling, but, particularly for the tropics, uncertainties are large and will depend crucially on possible changes to atmospheric dynamics in addition to increases in moisture content (e.g., O'Gorman 2012). In this context, the Ouagadougou event, during which both the moisture content and the low-level vorticity were at the top end of the present-day climatological distribution, points to an imminent need for future research: the investigation of strongly rotating, moisture-fueled vortices with a successive passage of MCSs that cause daily accumulations exceeding 200 mm. This can be achieved by 1) studying and modeling the dynamics of these and other recent cases with convection-permitting models and 2) by embedding the latter models into outputs of CMIP5 and upcoming CMIP6 models to carry out seasonal integrations to study future convective extreme events occurring in a warmer and more humid climate. The former approach will contribute to answering the question whether the superposition of several favorable forcing factors can create extreme outliers, as in the Ouagadougou case already under present climate conditions, while the latter will shed light on the question of whether multidecadal variations and global warming create variations in circulation and moisture content that cause different probabilities for extreme events (e.g., Trenberth et al. 2015). In either case, even century-long time series of daily rainfall would fail in statistically assessing century to millennia rainfall extremes for the future.

Acknowledgments. The second and third authors acknowledge partial support from the subproject “C2 – Prediction of wet and dry periods of the West African monsoon” of the Transregional Collaborative Research Center SFB/TRR 165 “Waves to Weather” funded by the German Science Foundation (DFG). We further thank Martin Stengel for providing SEVIRI images and acknowledge discussions with Jean-Philippe Lafore on the examined cases. Aïda Diongue Niang from the Senegalese National Weather Service ANACIM provided details on various rainfall intensities during the Dakar rainfall case. We also want to acknowledge the meteorological service of Burkina Faso, who provided the daily precipitation data for the Burkinabe stations from 1983 to 2010. The data are part of a novel precipitation database collected and quality controlled within the WASCAL research project (www.wascal.org) funded by the German Federal Ministry of Research and Education. The century-long time series for Dakar and Ouagadougou are available from the Karlsruhe African Surface Station–Database (KASS-D) from the Institute of Meteorology and Climate Research of the Karlsruhe Institute of Technology, Germany, and can be obtained upon request from the second author. We are grateful to Mr. Joseph Njeri, who processed the Burkinabe stations and created Figs. 1b and S1. We also thank three anonymous reviewers who helped to greatly improve the manuscript.

REFERENCES

- Adler, R. F., and Coauthors, 2003: The version-2 Global Precipitation Climatology Project (GPCP) monthly precipitation analysis (1979–present). *J. Hydrometeorol.*, **4**, 1147–1167, doi:10.1175/1525-7541(2003)004<1147:TVGPCP>2.0.CO;2.
- Ashouri, H., K.-L. Hsu, S. Sorooshian, D. K. Braithwaite, K. R. Knapp, L. D. Cecil, B. R. Nelson, and O. P. Prat, 2015: PERSIANN-CDR: Daily precipitation climate data record from multisatellite observations for hydrological and climate studies. *Bull. Amer. Meteor. Soc.*, **96**, 69–83, doi:10.1175/BAMS-D-13-00068.1.
- BBC News, 2009: UN warns on West Africa floods. Accessed 10 June 2015, <http://news.bbc.co.uk/2/hi/africa/8239552.stm>.
- Cook, K. H., and E. H. Vizy, 2015: Detection and analysis of an amplified warming of the Sahara Desert. *J. Climate*, **28**, 6560–6580, doi:10.1175/JCLI-D-14-00230.1.
- Cornforth, R. J., 2013: West African Monsoon 2012. *Weather*, **68**, 256–263, doi:10.1002/wea.2161.
- , and Coauthors, 2017: Synoptic systems. *Meteorology of Tropical West Africa: The Forecasters' Handbook*, D. J. Parker and M. Diop-Kane, Eds., Wiley-Blackwell, 40–89, doi:10.1002/9781118391297.ch2.
- Crétat, J., E. K. Vizy, and K. H. Cook, 2015: The relationship between African easterly waves and daily rainfall over West Africa: Observations and regional climate simulations. *Climate Dyn.*, **44**, 385–404, doi:10.1007/s00382-014-2120-x.
- Dee, D. P., and Coauthors, 2011: The ERA-Interim reanalysis: Configuration and performance of the data assimilation system. *Quart. J. Roy. Meteor. Soc.*, **137**, 553–597, doi:10.1002/qj.828.
- DFO, 2015: 2007 global register of major flood events. Dartmouth Flood Observatory, accessed 29 September 2015, <http://www.dartmouth.edu/~floods/Archives/2007sum.htm>.
- Dong, B., and R. Sutton, 2015: Dominant role of greenhouse-gas forcing in the recovery of Sahel rainfall. *Nat. Climate Change*, **5**, 757–760, doi:10.1038/nclimate2664.
- Douglas, I., K. Alam, M. Maghenda, Y. McDonnell, L. McLean, and J. Campbell, 2008: Unjust waters: Climate change, flooding and the poor in Africa. *Environ. Urban.*, **20**, 187–205, doi:10.1177/0956247808089156.
- Emanuel, K. A., 1994. *Atmospheric Convection*. Oxford University Press, 592 pp.
- EM-DAT, 2015: The OFDA/CRED International Disaster Database. Université Catholique de Louvain, accessed 29 September 2015, <http://www.emdat.be>.
- Fink, A. H., and A. Reiner, 2003: Spatiotemporal variability of the relation between African easterly waves and West African squall lines in 1998 and 1999. *J. Geophys. Res.*, **108**, 4332, doi:10.1029/2002JD002816.
- , and Coauthors, 2017: Mean climate and seasonal cycle. *Meteorology of Tropical West Africa: The Forecasters' Handbook*, D. J. Parker and M. Diop-Kane, Eds., Wiley-Blackwell, 1–39, doi:10.1002/9781118391297.ch1.
- Fortune, M., 1980: Properties of African squall lines from time-lapse satellite imagery. *Mon. Wea. Rev.*, **108**, 153–168, doi:10.1175/1520-0493(1980)108<0153:POASLI>2.0.CO;2.
- Galvin, J. F. P., 2010: Two easterly waves in West Africa in summer 2009. *Weather*, **65**, 219–227, doi:10.1002/wea.605.
- Gosset, M., J. Viarre, G. Quantin, and M. Alcoba, 2013: Evaluation of several rainfall products used for hydrological applications over West Africa using two high-resolution gauge networks. *Quart. J. Roy. Meteor. Soc.*, **139**, 923–940, doi:10.1002/qj.2130.
- Hardoy, J. E., D. Mitlin, and D. Satterthwaite, 2001: *Environmental Problems in an Urbanizing World: Finding Solutions in Cities in Africa, Asia and Latin America*. Earthscan, 464 pp.
- Hartill, L., 2008: Understanding West Africa's rising food prices. Catholic Relief Services, accessed 29 September 2015, <http://reliefweb.int/report/burkina-faso/understanding-west-african-rising-food-prices>.
- Hirabayashi, Y., R. Mahendran, S. Koirala, L. Konoshima, D. Yamazaki, S. Watanabe, H. Kim, and S. Kanae, 2013: Global flood risk under climate change. *Nat. Climate Change*, **3**, 816–821, doi:10.1038/nclimate1911.
- Hosking, J. R. M., 1996: Fortran routines for use with the method of L-moments, Version 3.04. Research Rep. RC-20525, IBM Research Division, 157 pp.
- , and J. R. Wallis, 1987: Parameter and quantile estimation for the generalized Pareto distribution. *Technometrics*, **29**, 339–349, doi:10.1080/00401706.1987.10488243.
- Hsu, K., X. Gao, S. Sorooshian, and H. V. Gupta, 1997: Precipitation estimation from remotely sensed information using artificial neural networks. *J. Appl. Meteor. Climatol.*, **36**, 1176–1190, doi:10.1175/1520-0450(1997)036<1176:PEFRSI>2.0.CO;2.
- , H. V. Gupta, X. Gao, and S. Sorooshian, 1999: Estimation of physical variables from multichannel remotely sensed imagery using a neural network: Application to rainfall estimation. *Water Resour. Res.*, **35**, 1605–1618, doi:10.1029/1999WR900032.
- Huffman, G. J., and Coauthors, 1997: The Global Precipitation Climatology Project (GPCP) combined precipitation dataset. *Bull. Amer. Meteor. Soc.*, **78**, 5–20, doi:10.1175/1520-0477(1997)078<0005:TGPCPG>2.0.CO;2.
- , R. F. Adler, M. M. Morrissey, D. T. Bolvin, S. Curtis, R. Joyce, B. McGavock, and J. Susskind, 2001: Global

- Precipitation at One-Degree daily resolution from multisatellite observations. *J. Hydrometeorol.*, **2**, 36–50, doi:10.1175/1525-7541(2001)002<0036:GPAODD>2.0.CO;2.
- , and Coauthors, 2007: The TRMM Multisatellite Precipitation Analysis (TMPA): Quasi-global, multiyear, combined-sensor precipitation estimates at fine scales. *J. Hydrometeorol.*, **8**, 38–55, doi:10.1175/JHM560.1.
- , R. F. Adler, D. T. Bolvin, and G. Gu, 2009: Improving the global precipitation record: GPCP Version 2.1. *Geophys. Res. Lett.*, **36**, L17808, doi:10.1029/2009GL040000.
- IPCC, 2007: *Climate Change 2007: Impacts, Adaptation and Vulnerability*. Cambridge University Press, 976 pp.
- , 2012: *Managing the Risks of Extreme Events and Disasters to Advance Climate Change Adaptation*. Cambridge University Press, 582 pp.
- , 2014: *Climate Change 2014: Impacts, Adaptation, and Vulnerability. Part A: Global and Sectoral Aspects*. Cambridge University Press, 1132 pp., doi:10.1017/CBO9781107415379.
- Jonkman, S. N., 2005: Global perspectives of loss of human life caused by floods. *Nat. Hazards*, **34**, 151–175, doi:10.1007/s11069-004-8891-3.
- Knapp, K. R., and Coauthors, 2011: Globally gridded satellite (GridSat) observations for climate studies. *Bull. Amer. Meteor. Soc.*, **92**, 893–907, doi:10.1175/2011BAMS3039.1.
- Lafore, J.-P., and Coauthors, 2011: Progress in understanding of weather systems in West Africa. *Atmos. Sci. Lett.*, **12**, 7–12, doi:10.1002/asl.335.
- , and Coauthors, 2017: Deep convection. *Meteorology of Tropical West Africa: The Forecasters' Handbook*, D. J. Parker and M. Diop-Kane, Eds., Wiley-Blackwell, 90–128, doi:10.1002/9781118391297.ch3.
- Lebel, T., A. Diedhiou, and H. Laurent, 2003: Seasonal cycle and interannual variability of the Sahelian rainfall at hydrological scales. *J. Geophys. Res.*, **108**, 8389, doi:10.1029/2001JD001580.
- Li, Z., F. Brissette, and J. Chen, 2013: Finding the most appropriate precipitation probability distribution for stochastic weather generation and hydrological modeling in Nordic watersheds. *Hydrol. Processes*, **27**, 3718–3729, doi:10.1002/hyp.9499.
- Liu, C. T., and E. J. Zipser, 2014: Differences between the surface precipitation estimates from the TRMM Precipitation Radar and passive microwave radiometer version 7 products. *J. Hydrometeorol.*, **15**, 2157–2175, doi:10.1175/JHM-D-14-0051.1.
- , —, D. J. Cecil, S. W. Nesbitt, and S. Sherwood, 2008: A cloud and precipitation feature database from nine years of TRMM observations. *J. Appl. Meteor. Climatol.*, **47**, 2712–2728, doi:10.1175/2008JAMC1890.1.
- Maggioni, V., P. C. Meyers, and M. D. Robinson, 2016: A review of merged high-resolution satellite precipitation product accuracy during the Tropical Rainfall Measuring Mission (TRMM) era. *J. Hydrometeorol.*, **17**, 1101–1117, doi:10.1175/JHM-D-15-0190.1.
- Martin, E., and C. Thorncroft, 2015: Representation of African easterly waves in CMIP5 models. *J. Climate*, **28**, 7702–7715, doi:10.1175/JCLI-D-15-0145.1.
- Mathon, V., H. Laurent, and T. Lebel, 2002: Mesoscale convective systems rainfall in the Sahel. *J. Appl. Meteor.*, **41**, 1081–1092, doi:10.1175/1520-0450(2002)041<1081:MCSRIT>2.0.CO;2.
- Miao, C., H. Ashouri, K.-L. Hsu, S. Sorooshian, and Q. Duan, 2015: Evaluation of the PERSIANN-CDR daily rainfall estimates in capturing the behavior of extreme precipitation events over China. *J. Hydrometeorol.*, **16**, 1387–1396, doi:10.1175/JHM-D-14-0174.1.
- Müller, C., K. Waha, A. Bondeau, and J. Heinke, 2014: Hotspots of climate change impacts in sub-Saharan Africa and implications for adaptation and development. *Global Change Biol.*, **20**, 2505–2517, doi:10.1111/gcb.12586.
- Nchito, W. S., 2007: Flood risk in unplanned settlements in Lusaka. *Environ. Urban.*, **19**, 539–551, doi:10.1177/0956247807082835.
- Nicholson, S. E., and Coauthors, 2003: Validation of TRMM and other rainfall estimates with a high-density gauge dataset for West Africa. Part I: Validation of GPCC rainfall product and pre-TRMM rainfall products. *J. Appl. Meteor.*, **42**, 1337–1354, doi:10.1175/1520-0450(2003)042<1337:VOTAOR>2.0.CO;2.
- Njau, L. N., and W. M. Thiaw, 2011: Western Africa [in “State of the Climate in 2010”]. *Bull. Amer. Meteor. Soc.*, **92** (6), S193–S194, doi:10.1175/1520-0477-92.6.S1.
- O’Gorman, P. A., 2012: Sensitivity of tropical precipitation extremes to climate change. *Nat. Geosci.*, **5**, 697–700, doi:10.1038/ngeo1568.
- Paeth, H., and A. Hense, 2005: Mean versus extreme climate in the Mediterranean region and its sensitivity to future global warming conditions. *Meteor. Z.*, **14**, 329–347, doi:10.1127/0941-2948/2005/0036.
- , A. H. Fink, S. Pohle, F. Keis, H. Mächel, and C. Samimi, 2011: Meteorological characteristics and potential causes of the 2007 flood in sub-Saharan Africa. *Int. J. Climatol.*, **31**, 1908–1926, doi:10.1002/joc.2199.
- Pfeifroth, U., J. Trentmann, A. H. Fink, and B. Ahrens, 2016: Evaluating satellite-based diurnal cycles of precipitation in the African tropics. *J. Appl. Meteor. Climatol.*, **55**, 23–39, doi:10.1175/JAMC-D-15-0065.1.
- Prakash, S., A. K. Mitra, I. M. Momin, D. S. Pai, E. N. Rajagopal, and S. Basu, 2015: Comparison of TMPA-3B42 versions 6 and 7 precipitation products with gauge-based data over India for the southwest monsoon period. *J. Hydrometeorol.*, **16**, 346–362, doi:10.1175/JHM-D-14-0024.1.
- Redl, R., A. H. Fink, and P. Knippertz, 2015: An objective detection method for convective cold pool events and its application to northern Africa. *Mon. Wea. Rev.*, **143**, 5055–5072, doi:10.1175/MWR-D-15-0223.1.
- Roca, R., P. Chambon, I. Jobard, P.-E. Kirstetter, M. Gosset, and J. C. Bergès, 2010: Comparing satellite and surface rainfall products over West Africa at meteorologically relevant scales during the AMMA campaign using error estimates. *J. Appl. Meteor. Climatol.*, **49**, 715–731, doi:10.1175/2009JAMC2318.1.
- Rodríguez-Fonseca, B., and Coauthors, 2011: Interannual and decadal SST-forced responses of the West African monsoon. *Atmos. Sci. Lett.*, **12**, 67–74, doi:10.1002/asl.308.
- Rowell, D. P., and J. R. Milford, 1993: On the generation of African squall lines. *J. Climate*, **6**, 1181–1193, doi:10.1175/1520-0442(1993)006<1181:OTGOAS>2.0.CO;2.
- Sane, Y., and Coauthors, 2012: An analysis of the diurnal cycle of precipitation over Dakar using local rain-gauge data and a general circulation model. *Quart. J. Roy. Meteor. Soc.*, **138**, 2182–2195, doi:10.1002/qj.1932.
- Sanogo, S., A. H. Fink, J. B. Omotosho, A. Ba, R. Redl, and V. Ermert, 2015: Spatio-temporal characteristics of the recent rainfall recovery in West Africa. *Int. J. Climatol.*, **35**, 4589–4605, doi:10.1002/joc.4309.
- Schmetz, J., P. Pili, S. Tjemkes, D. Just, J. Kerkman, S. Rota, and A. Ratier, 2002: An introduction to Meteosat Second Generation (MSG). *Bull. Amer. Meteor. Soc.*, **83**, 977–992, doi:10.1175/1520-0477(2002)083<0977:AITMSG>2.3.CO;2.

- Sima, F., A. Kamga, I. Raiva, S. F. Dekaa, and A. I. James, 2013: West Africa [in “State of the Climate in 2012”]. *Bull. Amer. Meteor. Soc.*, **94** (8), S164–S166, doi:[10.1175/2013BAMSStateoftheClimate.1](https://doi.org/10.1175/2013BAMSStateoftheClimate.1).
- Tarhule, A., 2005: Damaging rainfall and flooding: The other Sahel hazards. *Climatic Change*, **72**, 355–377, doi:[10.1007/s10584-005-6792-4](https://doi.org/10.1007/s10584-005-6792-4).
- Trapp, R. J., 2013: *Mesoscale-Convective Processes in the Atmosphere*. Cambridge University Press, 377 pp.
- Trenberth, K. E., J. T. Fasullo, and T. G. Shepherd, 2015: Attribution of climate extreme events. *Nat. Climate Change*, **5**, 725–730, doi:[10.1038/nclimate2657](https://doi.org/10.1038/nclimate2657).
- Tschakert, P., R. Sagoe, G. Ofori-Darko, and S. N. Codjoe, 2010: Floods in the Sahel: An analysis of anomalies, memory, and anticipatory learning. *Climatic Change*, **103**, 471–502, doi:[10.1007/s10584-009-9776-y](https://doi.org/10.1007/s10584-009-9776-y).
- UNDP, 2015: World urbanization prospects: The 2014 revision. ST/ESA/SER.A/366, United Nations, 32 pp., <https://www.compassion.com/multimedia/world-urbanization-prospects.pdf>.
- World Water Assessment Programme, 2009: Water in a changing world. United Nations World Water Development Rep. 3, 318 pp., <http://unesdoc.unesco.org/images/0018/001819/181993e.pdf>.
- Zulkafli, Z., W. Buytaert, C. Onof, B. Manz, E. Tarnavsky, W. Lavado, and J.-L. Guyot, 2014: Comparative performance analysis of TRMM 3B42 (TMPA) versions 6 and 7 for hydrological applications over Andean–Amazon River basins. *J. Hydrometeor.*, **15**, 581–592, doi:[10.1175/JHM-D-13-094.1](https://doi.org/10.1175/JHM-D-13-094.1).